Augmenting Vertical Energy Entrainment within Wind Farms via Lifting Devices

Augmenting Vertical Energy Entrainment within Wind Farms via Lifting Devices

YuanTso Li[1], **Andrea Sciacchitano**[1], **and Wei Yu**[1]
[1]Faculty of Aerospace Engineering, Delft University of Technology, Delft, the Netherlands
E-mail: Y.Li-18@tudelft.nl

Abstract. This study evaluates the addition of lifting devices (LDs) in conventional wind farms as a practical step toward realizing the concept of regenerative wind farm (RGWF). RANS-based CFD simulations are performed to investigate multiple spatial arrangements of LDs within wind farms. The results show that installing LDs between turbines can substantially increase wind farm power output by more than 80%, further supporting the concept of RGWF. It is found that the tandem placements outperform the staggered ones. Moreover, the up-washing LDs are considered more effective than the down-washing ones in terms of vertical energy entraining capabilities. Although clear trends emerge, the study is limited by large uncertainties associated with RANS turbulence models, making quantitative assessments rather challenging. Experimental testing and simulations using higher-fidelity numerical methods are recommended for future work to yield more quantitative outcomes.

1. Introduction

Previous studies have shown that integrating wind energy harvesters with large-scale wing structures can substantially increase the land-use efficiency [1, 2]. For wind farms (WFs) of equal size, those equipped with wing structures (lifting device) can extract roughly twice the power of conventional farms [1, 2]. This improvement is due to the enhanced vertical energy entrainment facilitated by the lifting devices' (LDs') tip-vortex-induced vertical flows [1–5]. In this work, wind farms incorporating such wing structures are referred to as regenerative wind farms (RGWFs) [6].

Although the reported performance of RGWFs is promising, the wind energy systems considered in the earlier studies [1–5], namely the multi-rotor systems with lifting device (MRSL), have not yet been realized at utility scale. While MRSL may be technically feasible [7, 8], deploying technologies that differ substantially from current commercial designs faces strong industrial inertia and may introduce intolerable risks [9]. Therefore, advancing the RGWF concept through lower-risk intermediate steps is strongly desired. Such steps can demonstrate feasibility before the concept is fully realized using radically distinct wind energy harvesters.

As noted in the previous works [1, 2], the essential feature of RGWF is not the specific type of wind energy harvester but the integration of LDs. Accordingly, those studies proposed installing LDs in the inter-turbine spaces of existing wind farms as a practical intermediate step toward realizing the RGWF concept. In other words, they proposed converting existing WFs into RGWFs rather than building new ones from scratch. This approach is more feasible since it avoids the need to install new turbine systems (either conventional wind turbines or MRSLs) and

requires only the addition of LDs. Its effectiveness can also be directly assessed by comparing WF's performance before and after the installation of LDs. Motivated by these considerations, this study evaluates the RGWF concept using CFD (computational fluid dynamics) simulations of WFs with and without LDs placed between turbines. Additionally, multiple simulations with different spatial arrangements of LDs are conducted in an attempt to identify the most effective deployment strategy. Note that, rather than employing higher-fidelity numerical methods, Reynolds-averaged Navier-Stokes (RANS) approaches are adopted in the present work, enabling the exploration of larger parameter spaces with the available computational resources.

2. Description of the wind turbine and the lifting device

The wind turbine (WT) used in this study follows the specifications of the Vestas V-80 deployed at the Horns Rev offshore wind farm [10]. V-80 has a rotor diameter of $D = 80$ m and a hub height of $z_{\text{hub}} = 70$ m. The lifting device consists of four straight wings, each with a span equal to D and a chord of $c = D/8$. All wings use the S1223 airfoil profile [11] along their full span, and their vertical positions are $z = [z_{\text{hub}} - 0.25D, z_{\text{hub}} + 0.00D, z_{\text{hub}} + 0.25D, z_{\text{hub}} + 0.50D]$. These parameters are selected such that the lift force generated by the LDs is comparable to the thrust of the wind energy harvesters (see Figure 5); note that previous studies [1, 2] have demonstrated that the concept of RGWF can be effective with this design.

3. Description of the wind farm layouts

The wind farm layouts in this study follow that of the Horns Rev offshore wind farm [10], which has been extensively analyzed in previous works [12, 13]. To reduce computational cost, scaled-down WFs with 7×5 turbines instead of the full 10×8 are simulated, as shown in Figure 1(a). Consistent with Horns Rev, the turbine spacings are $7D$ in both the streamwise and lateral directions, with a 7° inclination between adjacent columns. Only westerly inflow is considered, making the successive WTs rows fully aligned with the inflow direction, as illustrated in Figure 1.

In addition to the reference configuration (no LDs), five spatial arrangements of LDs are examined to identify the superior placement strategy (see Table 2 for their configuration labels). The first overlaps the locations of LDs and WTs (termed *Integrated*, Fig. 1(b)), equivalent to the MRSL concept in [1, 2] and serving as secondary references. The second positions LDs $3.5D$ downstream away from the turbines (termed *Tandem*, Figure. 1(c)). The third locates LDs between both the turbine rows and columns (termed *Staggered*, Figure. 1(d)). The fourth and fifth configurations follow the Tandem and Staggered layouts but include an additional upstream row of LDs (the red pluses in Figures 1(c) and 1(d)). Notice that, except for the added upstream row of LDs, all other LDs lie within the original WF footprint.

4. Methodology

This work closely follows the methodology of Li et al. [1]. Therefore, for brevity, only the elements that are critical or specific to the present study are detailed here. Readers are referred to that work for further documentation. Additionally, all simulation settings used in this study are also provided in the accompanying data repository [14]. It is worth mentioning that this work does not intend to capture the near wake aerodynamics of WTs and LDs; instead, integral quantities at the far wake regions ($> 4D$ downstream away from WTs or LDs) are focused.

4.1. Modeling of the aerodynamic of wind turbines and the lifting devices

The wind turbines are modeled as circular actuator disks with 25 actuator elements across the rotor diameter. For simplicity, only the streamwise forces are applied, which are determined from the local flow conditions sampled by the actuator elements. A thrust coefficient $C_T = 0.80$ is prescribed by setting the modified thrust coefficient to $C_T^* = 1.53$, obtained from the relation

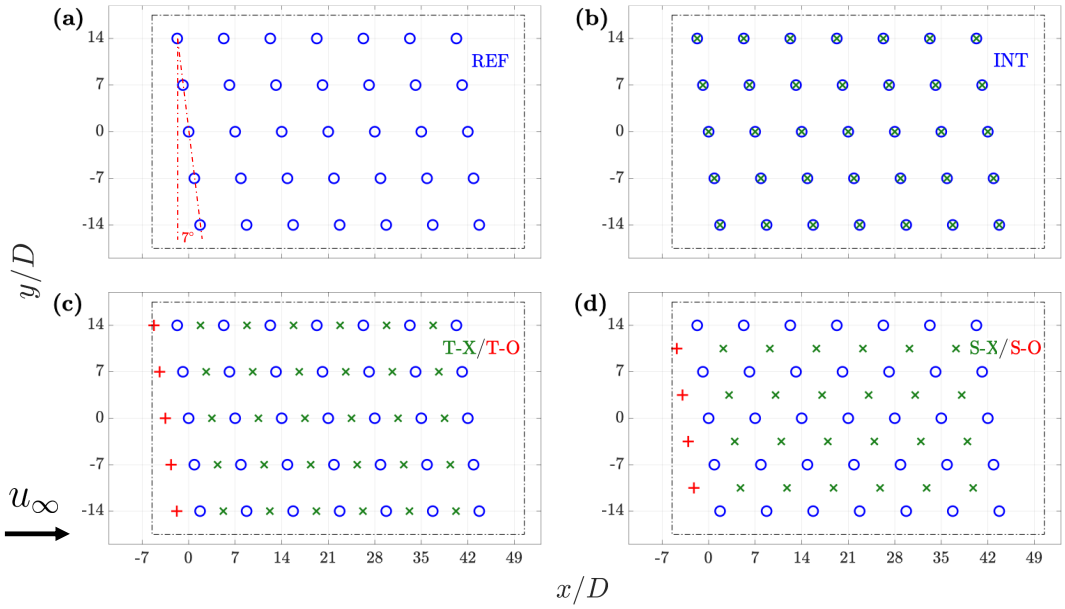

Figure 1. Sketches of the wind farm layouts. Configuration labels corresponding to Table 2 are shown in the top-right corner of each panel. Blue circles mark the positions of wind turbines, while green crosses and red pluses indicate the locations of the lifting devices. The lifting devices shown as red pluses are included only in configurations with the suffix "O".

Table 1. Boundary conditions of the current simulations. `atmBoundaryLayer` and `WallFunction` are abbreviated to `ABL` and `WF`. The value of `uniformFixedValue` for pressure is that of the ambient.

	Inlet	Outlet	Ground	Top	Sides
$\boldsymbol{u}$	`ABLInletVelocity`	`inletOutlet`	`noSlip`	`zeroGradient`	`zeroGradient`
p	`zeroGradient`	`uniformFixedValue`	`zeroGradient`	`uniformFixedValue`	`uniformFixedValue`
k	`ABLInletK`	`zeroGradient`	`kqRWF`	`zeroGradient`	`zeroGradient`
ω	`ABLInletOmega`	`zeroGradient`	`omegaWF`	`zeroGradient`	`zeroGradient`
ϵ	`ABLInletEpsilon`	`zeroGradient`	`epsilonWF`	`zeroGradient`	`zeroGradient`
ν_T	`calculated`	`calculated`	`atmNutkWF`	`calculated`	`calculated`

$C_T^* = C_T/(1-a)^2$ based on one-dimensional momentum theory [15, 16]. Here, a is the axial induction factor and has a value of 0.276 by solving $C_T = 0.8 = 4a(1-a)$. Note that $C_T = 0.80$ is consistent with that of the Vestas V-80 turbines [10, 13]. Turbine power is calculated by summing the inner products of the local velocity and force vectors at the actuator elements.

Each lifting device is modeled using four actuator lines. The airfoil polar of S1223 [11] is used, and the pitch angles are adjusted during the simulations so that the mid-span angle of attack yields a lift coefficient of $C_l = 2.2$. Further details can be found in Li et al. [1].

4.2. General numerical setup

The simulations are performed using *OpenFOAM v2506* [17], following the general framework of Li et al. [1]. Two RANS models are employed for turbulence closure, which are $k-\omega$ SST [18] model and realizable $k-\epsilon$ model [19]. The inflow is modeled as a neutral atmospheric surface layer using the library `atmosphericModels` [17, 20, 21] with its implementations described in Equation 1. Here, u and k denote the streamwise velocity and turbulent kinetic energy. The reference height $z_{\text{ref}} = z_{\text{hub}}$, reference velocity $u_\infty = 10$ m/s, and surface roughness $z_0 = 10^{-4}$ m

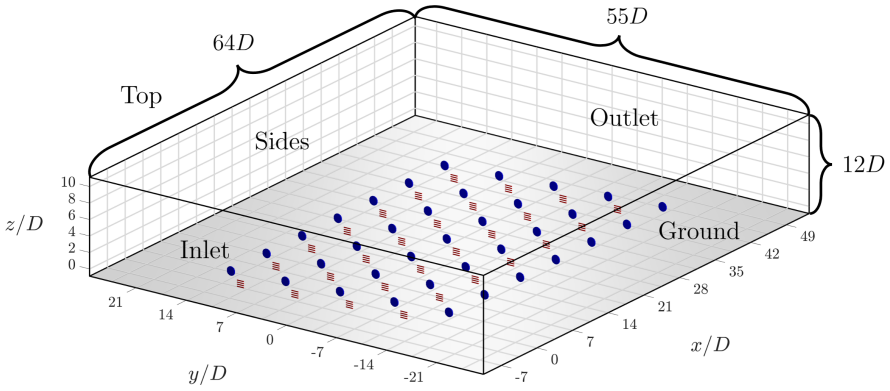

Figure 2. Sketch of the computational domain. Wind turbines (actuator disks) and lifting devices (actuator lines) are represented by blue and red surfaces, respectively. The inflow enters from the bottom left. The configuration shown in this figure corresponds to the staggered layout with an additional upstream row of LDs (U-S-O or D-S-O).

are set. The model constants κ, C_μ, C_1, and C_2 are set to 0.41, 0.09, 0.642, and 1.0, respectively. Under these conditions, the inflow turbulence intensity, $\mathrm{TI}_\infty \triangleq \sqrt{2k/3}/u_\infty$, is 8% at $z = z_{\mathrm{ref}}$, following the typical offshore conditions [22].

$$u(z) = \frac{u^*}{\kappa} \ln\left(\frac{z+z_0}{z_0}\right), \quad u^* = \frac{u_\infty \kappa}{\ln\left(\frac{z_{\mathrm{ref}}+z_0}{z_0}\right)}, \quad k(z) = \frac{(u^*)^2}{\sqrt{C_\mu}} \sqrt{C_1 \ln\left(\frac{z+z_0}{z_0}\right) + C_2} \tag{1}$$

The computational domain and boundary conditions are shown in Figure 2 and summarized in Table 1. A Cartesian coordinate system is used, with the origin located at the rotor center of the first-row-center-column WT (see Figure 1). For cases with and without an additional upstream row of LDs, the origin is located $10.5D$ and $8.0D$ downstream from the inlet, respectively. The domain extends $64D$, $55D$, and $12D$ in the streamwise, lateral, and vertical directions. A refined subdomain of $64D \times 41D \times 5D$ has a uniform cell size of $D/25$. Ten layers of cells are placed near the bottom $0.055D$ with an expansion ratio of 1.8. Grid spacing increases gradually toward the boundaries from the refined subdomain, with the lateral and vertical expansion ratios being 1.14 and 1.10, respectively. The total mesh contains 238.8 million cells.

5. Test matrix

A total of eleven wind farm configurations are analyzed in this study, as listed in Table 2. One of the configurations is without LDs, which serves as the reference configuration (REF). The remaining ten configurations are grouped according to whether the LDs induce upward (up-washing) or downward (down-washing) flows right behind them. Each group includes five LD placement patterns described in Section 3. All configurations are simulated with two turbulence models, namely $k-\omega$ SST [18] and realizable $k-\epsilon$ [19], to assess model-related uncertainties in the RANS framework.

6. Results and discussions

6.1. Power performance

The normalized row-averaged turbine power is denoted as $< \widehat{P}^R >$, where $< \cdot >$ indicates the row-averaging and $\widehat{\cdot}$ denotes the normalization. The values are normalized by the row-averaged

Table 2. Test matrix of the current study. Visual representations of the corresponding wind farm configurations are shown in Figure 1, where the positions of WTs and LDs are indicated.

Configuration label	LD configuration	LD placement	Extra front row of LD
REF	N.A.	N.A.	N.A.
U-INT	Up-Washing	Integrated	N.A.
U-T-X	Up-Washing	Tandem	No
U-T-O	Up-Washing	Tandem	Yes
U-S-X	Up-Washing	Staggered	No
U-S-O	Up-Washing	Staggered	Yes
D-INT	Down-Washing	Integrated	N.A.
D-T-X	Down-Washing	Tandem	No
D-T-O	Down-Washing	Tandem	Yes
D-S-X	Down-Washing	Staggered	No
D-S-O	Down-Washing	Staggered	Yes

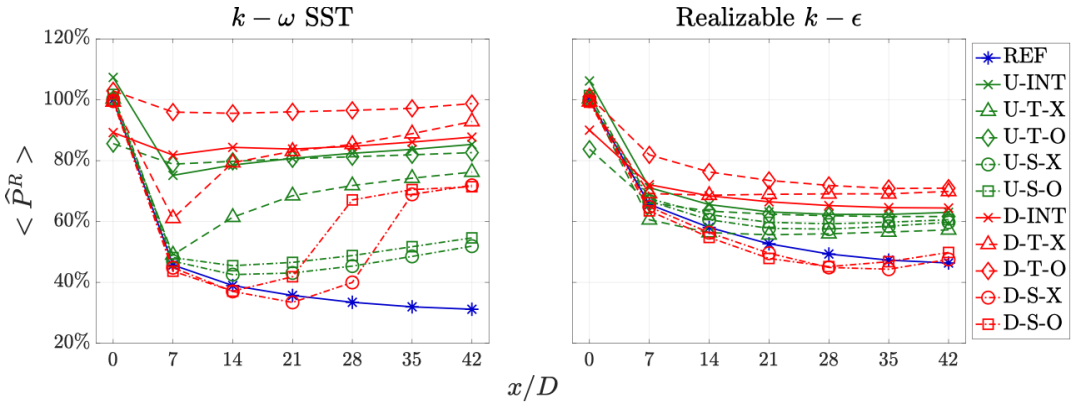

Figure 3. Normalized row-averaged turbine power, $< \widehat{P}^R >$, for all eleven configurations listed in Table 2. Outcomes of both turbulence models ($k-\omega$ SST and realizable $k-\epsilon$) are shown.

first-row-power of the reference case $< P^R_{\mathrm{REF}} >_{1^{\mathrm{st}}}$ as defined in Equation (2). The resulting $< \widehat{P}^R >$ for all eleven configurations in Table 2 with both turbulence models are shown in Figure 3. In addition, the total wind farm power output P_{WF} for each case is presented with the histogram in Figure 4. For reference, $< P^R_{\mathrm{REF}} >_{1^{\mathrm{st}}}$ predicted by $k-\omega$ SST and realizable $k-\epsilon$ are 1.82 MW and 1.86 MW, respectively, which are very close to the 1.78 MW predicted by the one-dimensional momentum theory. Moreover, the corresponding total farm power for the REF configuration is 28.9 MW with $k-\omega$ SST and 39.0 MW with realizable $k-\epsilon$, respectively.

$$< \widehat{P}^R > \stackrel{\Delta}{=} \frac{< P^R >}{< P^R_{\mathrm{REF}} >_{1^{\mathrm{st}}}} \tag{2}$$

Focusing on the REF configuration, the predicted $< \widehat{P}^R >$ for turbines in the 2^{nd} to 7^{th} rows decreases from about 45% to 30% with the $k-\omega$ SST model and from 65% to 45% with the realizable $k-\epsilon$ model. These values are substantially lower than field measurements [12] and large-eddy simulation results [13], where $< \widehat{P}^R >$ plateaus beyond the 2^{nd} row at approximately 60% and 55%, respectively. These discrepancies highlight the limitations of the present CFD framework arising from the RANS approaches. The large differences between the two turbulence

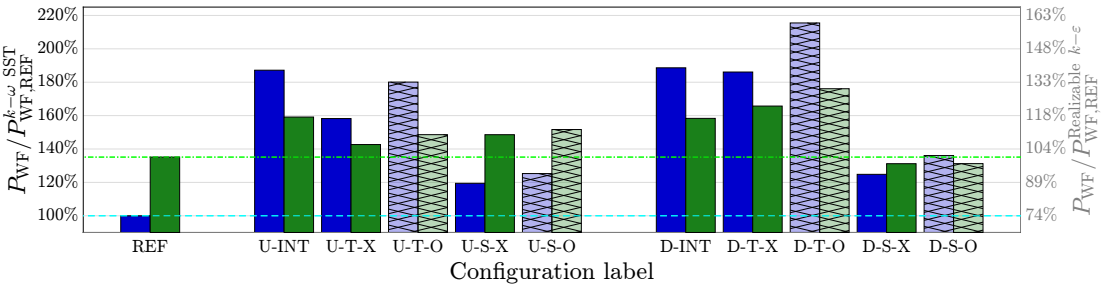

Figure 4. Histogram of the wind farm power output P_{WF} for the eleven configurations in Table 2. The results obtained with both turbulence models ($k-\omega$ SST and realizable $k-\epsilon$) are shown. Blue and green bars correspond to predictions from the $k-\omega$ SST and realizable $k-\epsilon$, respectively. The left and right Y-axis are normalized by the power output of REF for each model, denoted as $P^{k-\omega\ \mathrm{SST}}_{\mathrm{WF,\ REF}}$ and $P^{\mathrm{Realizable}\ k-\epsilon}_{\mathrm{WF,\ REF}}$, respectively, and their 100% are marked with horizontal dotted-dashed lines. For improved visual contrast, configurations that include an additional upstream row of LDs are indicated by hatched bars.

models stem from that the realizable $k-\epsilon$ model predicts significantly larger eddy viscosity ν_T for the current application (see Appendix B of Li et al. [1]), leading to higher diffusivity.

Although the realizable $k-\epsilon$ model yields results for the REF configuration that align more closely with the field measurements and LES predictions, the present analysis focuses more on $k-\omega$ SST. This choice is motivated by the observation that, compared with LES predictions [5], the LD-induced swirling flows predicted by realizable $k-\epsilon$ model seem to be too diffusive. The high eddy viscosity predicted by realizable $k-\epsilon$ overly weakens the LD-induced flow structures as the flow progresses, causing the predicted P^R values across the eleven configurations to appear more uniform compared to those obtained with $k-\omega$ SST.

Shifting back the focus to Figure 3, based on the reported P^R for different configurations, it can be seen that installing LDs effectively mitigates power losses for the downstream machines, either the LDs are configured in up-washing or down-washing. This effect is particularly pronounced in the results of $k-\omega$ SST, where $<\widehat{P}^R>$ is maintained at approximately 80% for several configurations. Moreover, an interesting feature is observed for the down-washing-staggered configurations in the same figure. Particularly, although they exhibit relatively low $<\widehat{P}^R>$ in the upstream rows, their performance gradually improves along the downstream, indicating the latent potential. This behavior arises for two main reasons. First, in the staggered layout, the vortical structures generated by the LDs interact less directly with the WT wakes, requiring additional downstream distance for effective coupling. Second, the strength of these vortical structures accumulates along successive rows [1], progressively reinforcing the interaction and ultimately promoting strong vertical mixing between the WT wakes and the higher-altitude flow (see Figure 6 for further details).

In terms of wind farm power enhancement, Figure 4 shows that configurations with LDs can substantially increase P_{WF}, particularly in the results obtained through $k-\omega$ SST; several configurations achieve gains exceeding 80%. However, for the cases using realizable $k-\epsilon$ model, the gains of P_{WF} provided by the LDs can drop to single-digit percentages. Figure 4 further indicates that LDs placed in tandem outperform those placed in staggered. Configurations that include an additional upstream row of LDs also tend to perform better, providing up to another 10% increase in P_{WF}. Moreover, the power outputs of the integrated configurations more closely resemble those in tandem than those in staggered. Furthermore, although the down-washing cases appear to be more favorable than the up-washing in terms of P_{WF}, this does not necessarily mean they are superior, which is further elaborated in the later section with flow-field analysis.

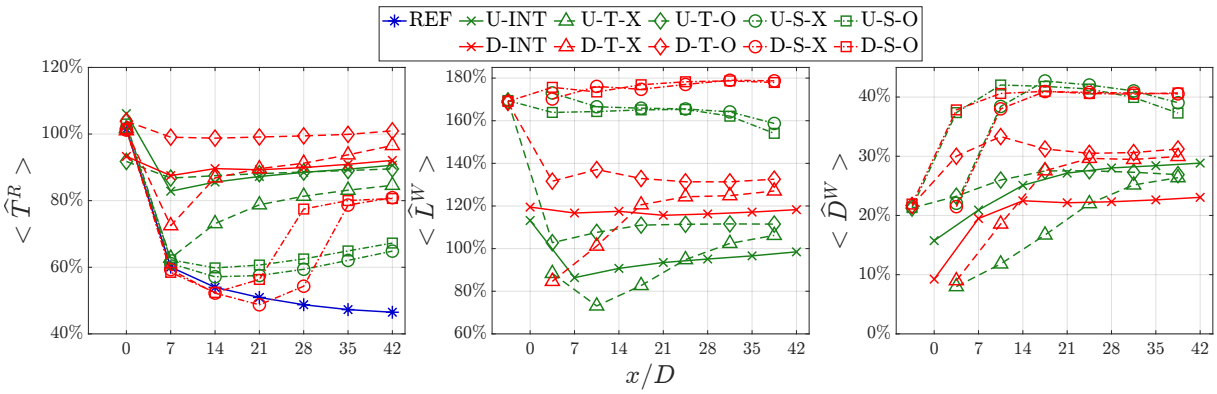

Figure 5. Normalized row-averaged WTs' thrust $< \widehat{T}^R >$, LDs' lift $< \widehat{L}^W >$, and LDs' drag $< \widehat{D}^W >$ for all eleven configurations listed in Table 2. Only the outcomes with $k-\omega$ SST model are shown.

6.2. Loading of the wind turbine rotors and the lifting devices

The normalized row-averaged WTs' thrust, LDs' lift, and LDs' drag are denoted as $< \widehat{T}^R >$, $< \widehat{L}^W >$, and $< \widehat{D}^W >$, respectively. These values are normalized by the row-averaged thrust force of the REF configuration evaluated at the first row, as defined in Equation (3). Here, T^R and D^W represent the streamwise components of the forces on the WTs and LDs, while L^W is the vertical force component on the LDs. The resulting normalized quantities for all eleven configurations are shown in Figure 5, with only the $k-\omega$ SST results presented for brevity. For reference, the thrust coefficients C_T computed based on $< T^R_{\text{REF}} >_{1^{\text{st}}}$ predicted by $k-\omega$ SST and realizable $k-\epsilon$ are 0.80 and 0.81, respectively. These values agree very well with that of 0.80 predicted by the one-dimensional momentum theory based on the relation between C^*_T and C_T, reaffirming the validity of the current actuator disk model.

$$< \widehat{T}^R > \triangleq \frac{< T^R >}{< T^R_{\text{REF}} >_{1^{\text{st}}}}, < \widehat{L}^W > \triangleq \frac{< |L^W| >}{< T^R_{\text{REF}} >_{1^{\text{st}}}}, < \widehat{D}^W > \triangleq \frac{< D^W >}{< T^R_{\text{REF}} >_{1^{\text{st}}}} \tag{3}$$

Figure 5 shows that L^W is the largest for the configurations in which the LDs are staggered relative to WTs. This is expected, as these LDs generally operate outside the turbine wakes. However, opposing to the findings of Li et al. [1], higher L^W do not directly translate into higher T^R and P^R for these configurations. This is primarily because the vortical structures generated by the staggered LDs are not aligned with the WTs' wakes, leading to weaker wake re-energization, as supported by the flow-field presented in Section 6.3.

The drag forces on the LDs (primarily induced drag), denoted D^W, are also shown in Figure 5. Although the LDs introduce substantial drag, the corresponding T^R and P^R results demonstrate that LD-equipped wind farms can still deliver more power despite this additional adverse loading.

6.3. Flow field analysis with velocity fields

This section presents the flow fields of the simulation cases using streamwise velocity contours. The results from $k-\omega$ SST and realizable $k-\epsilon$ models are shown in Figures 6 and 7, respectively. Except for the plane illustrating the inflow profile at $x/D = -5.5$, all contour planes are sampled at $x/D = 40.0$, located $2D$ upstream from the 7^{th}-row WTs.

For the cases simulated with $k-\omega$ SST, the influence of the LDs is clearly visible. Compared with the REF configuration, configurations with LDs exhibit strong in-plane velocity components, whereas those for REF are very limited. This lack of cross-stream flow in REF

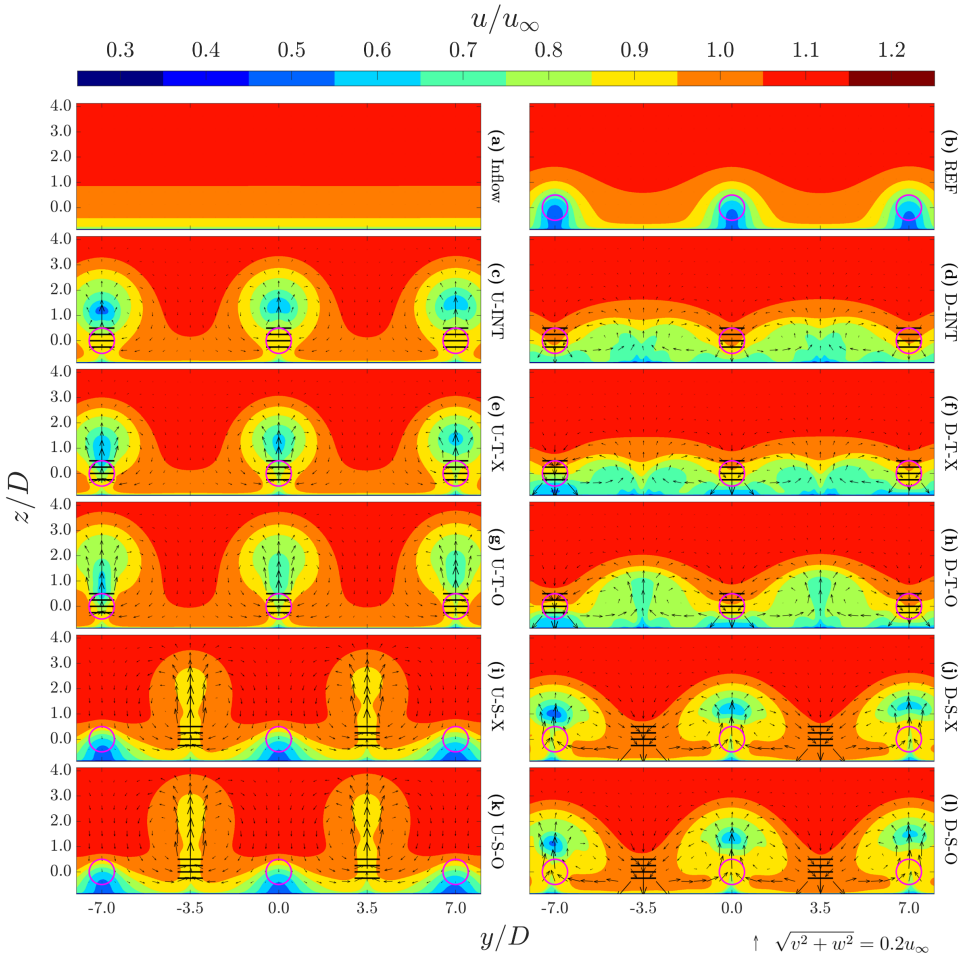

Figure 6. Contour plots of the streamwise velocity u for simulations using $k-\omega$ SST model. (a): u at plane $x/D = -5.5$ for REF configuration. (b–l): u at plane $x/D = 40.0$ for all eleven configurations listed in Table 2. In-plane velocities (v and w) are indicated with arrows and their scale is provided at the bottom right; these arrows are not visible in panels (a–b) because their magnitudes approach zero.

leads to weaker vertical mixing, reduced vertical energy entrainment, and WTs after the first row are completely immersed in the wakes of upstream turbines.

On the other hand, for the configurations with LDs, the up-washing ones generate pronounced upward flow right behind the LDs, while the down-washing ones produce clear downdrafts. An interesting observation is that staggered-down-washing configurations produce flow patterns resembling those of tandem-up-washing; however, the reverse does not hold. In staggered-up-washing configurations, the upward motion behind the LDs is strong enough to draw in the WT wakes from the sides and lift the low-momentum flow upward. In contrast, tandem-down-washing configurations mainly deflect turbine wakes sideways, trapping them at lower altitudes. This observation underscores the reduced ability to promote vertical mixing for the down-washing cases, a statement reinforced later with the quantitative vertical energy-flux analysis.

Looking into the flow fields obtained with the realizable $k-\epsilon$ model, it can be seen that the cases generally share similar features compared to those of the $k-\omega$ SST model. However,

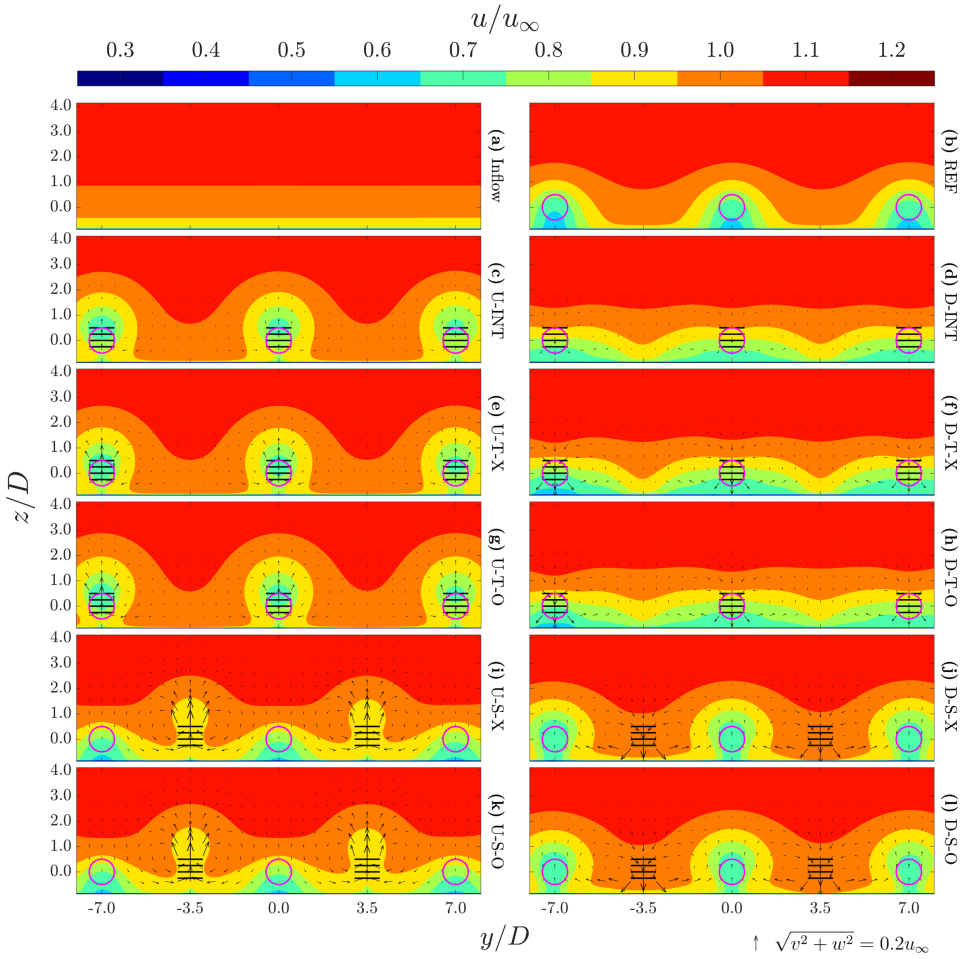

Figure 7. Contour plots of the streamwise velocity u for simulations using realizable $k-\epsilon$ model. (a): u at plane $x/D = -5.5$ for REF configuration. (b–l): u at plane $x/D = 40.0$ for all eleven configurations listed in Table 2.

the strengths of the swirling motions are much weaker. This is mainly due to the fact that ν_T predicted by the realizable $k-\epsilon$ model is generally much higher than that of the $k-\omega$ SST model (see Appendix B of Li et al. [1]). The higher ν_T smooths the velocity gradients and diffuses the vorticity more quickly, making the REF configuration less affected by wake interactions and diminishing the efficacy of LDs in cases where they are installed.

6.4. Altitude variations of vertical energy entrainment rate

This section examines the mechanical energy flux through the plane $\Omega_z \in [-5.5 \leq x/D \leq 50.5, -17.5 \leq y/D \leq 17.5]$ at various heights, denoted as Φ_z^{Total} and defined in Equation (4). The plane Ω_z is outlined by the dotted-dashed rectangles in Figure 1 and $\hat{n}_j$ is a unit vector pointing in positive z-direction. Also, note that the repeated indices are summed over. For clarity and focus, only configurations without the additional upstream row of LDs are included in Figure 8.

$$\Phi_z^{\text{Total}}(z) \triangleq \rho \oiint_{\Omega_z} \Bigg(\underbrace{-u_j K}_{\text{Advection},\Phi_z^{\text{Adv.}}} \quad \underbrace{+u_i\Big(2\nu S_{ij} + \tau_{ij}\Big)}_{\text{Diffusion},\Phi_z^{\text{Diff.}}} \quad \underbrace{-\frac{u_j p}{\rho}}_{\text{Pressure work}} \quad \underbrace{-u_j k + \left[\Big(\nu + \nu_T\Big)\frac{\partial k}{\partial x_j}\right]}_{\text{TKE advection plus diffusion}} \Bigg) \hat{n}_j \, \mathrm{d}x\mathrm{d}y \tag{4}$$

$$S_{ij} \triangleq \frac{1}{2}\left(\frac{\partial u_i}{\partial x_j} + \frac{\partial u_j}{\partial x_i}\right), \qquad \tau_{ij} = 2\nu_T S_{ij} - \frac{2}{3}k\delta_{ij} \tag{5}$$

Consistent with Li et al. [1], Figures 8(a–c) show that $\Phi_z^{\text{Total}} \simeq \Phi_z^{\text{Adv.}} + \Phi_z^{\text{Diff.}}$, indicating that vertical energy entrainment is dominated by advection and modeled turbulent diffusion. Although $\Phi_z^{\text{Adv.}}$ and $\Phi_z^{\text{Diff.}}$ are already able to separate the contributions of different mechanisms quantitatively, the raw values of $\Phi_z^{\text{Adv.}}$ can be misleading because they remain strongly negative even at higher z. These negative values do not indicate reduced vertical entrainment; rather, they arise from the continuity constraint. As the wind farm decelerates the flow, the expanding wakes induce upward flow above the farm, which leads to negative values of $\Phi_z^{\text{Adv.}}$ even at high altitude. The more the wind farms slow down the flow, the more negative the values of $\Phi_z^{\text{Adv.}}$ are. That is, with $z \gg z_{\text{hub}}$, higher P_{WF} generally correlated with more negative $\Phi_z^{\text{Adv.}}$. Therefore, direct comparison of the raw advective flux between configurations is potentially misleading as the negative values of $\Phi_z^{\text{Adv.}}$ are more associated with higher wind farm power extraction instead of lower vertical energy entrainment rate.

To enable fair comparison across configurations, $\Phi_z^{\text{Adv.}}$ is shifted by its value sampled at $z/D = 5.0$, yielding the corrected advection flux $\Phi_z^{\text{Adv.,Corr.}}$, which is defined in Equation (6). This correction is physically justified because $\Phi_z^{\text{Adv.}}$ generally reach their asymptotic levels (i.e., $\partial\Phi_z^{\text{Adv.}}/\partial z \simeq 0$) by $z/D = 4.0$, as shown in Figure 8.

$$\Phi_z^{\text{Adv., Corr.}}(z) \triangleq \Phi_z^{\text{Adv.}}(z) - \Phi_z^{\text{Adv.}}\Big|_{z=5.0D} \tag{6}$$

Comparing $\Phi_z^{\text{Diff.}}$ and $\Phi_z^{\text{Adv.}}$ shows that, except for the REF configuration, Φ_z^{Total} is dominated by advection process. This indicates that introducing LDs fundamentally alters the mechanism of vertical energy entrainment. Moreover, $\Phi_z^{\text{Adv.,Corr.}}$ is several factors larger than $\Phi_z^{\text{Diff.}}$, underscoring the strong influence of the LDs. Among the LD-equipped configurations, up-washing arrangements generally entrain more energy across $z/D = 0.5$ (the rotor-top height) through term $\Phi_z^{\text{Adv.,Corr.}}$, with the staggered configurations being the exception (however, the staggered-up-washing configuration is found to have larger $\Phi_z^{\text{Adv.,Corr.}}$ in higher altitudes). The smaller $\Phi_z^{\text{Adv.,Corr.}}$ observed in the down-washing configurations is consistent with the velocity contours in Figure 6, where these configurations tend to trap the exhausted wakes between the adjacent columns rather than ventilating them upward (again, with the staggered-down-washing configurations being the exception).

Based on these observations, this study concludes that, at least within the examined parameter space, up-washing configurations are more favorable than down-washing ones. Although some down-washing cases may deliver higher wind farm power output (see Figure 4), their tendency for WT wakes to remain trapped at lower altitudes and smaller $\Phi_z^{\text{Adv.,Corr.}}$ make them less desirable overall (see Figures 6 and 8).

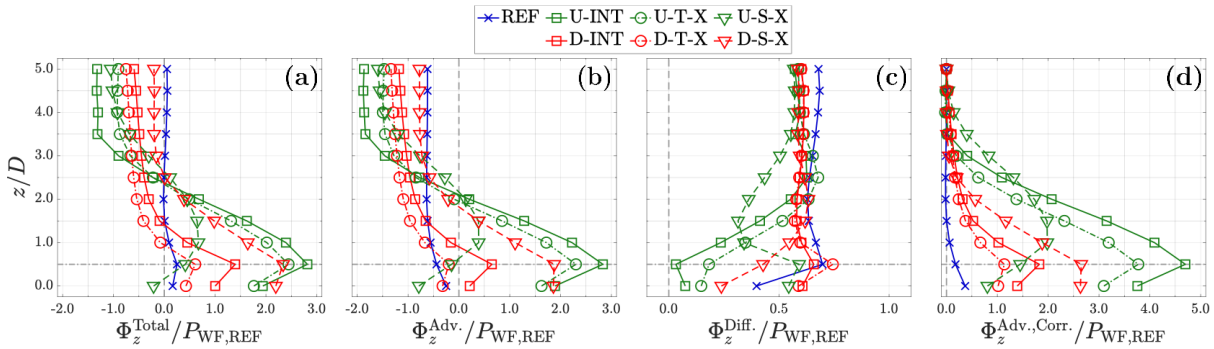

Figure 8. Vertical energy fluxes (see Equation 4) for the selected configurations performed with $k-\omega$ SST. (a): Total vertical energy flux, Φ_z^{Total}. (b): Contributions of advective terms, $\Phi_z^{\text{Adv.}}$. (c): Contributions of the diffusion terms, $\Phi_z^{\text{Diff.}}$. (d): Corrected advective contributions, $\Phi_z^{\text{Adv.,Corr.}}$ (see Equation 6). The dotted-dashed lines indicate the rotor top's height.

7. Conclusions and outlooks

Introducing lifting devices (LDs) into existing conventional wind farms can be a feasible intermediate step toward realizing the concept of regenerative wind farm (RGWF), a concept that can substantially reduce wake-induced wind farm power losses. The highlight of this strategy is that it does not require deploying new wind-energy systems that are drastically different from the current mainstream designs. Motivated by this idea, the present study employed RANS-based CFD simulations to assess the impacts of installing LDs into wind farms that closely followed the layout of an existing one. The LDs were placed either in tandem with or staggered relative to the turbines, and their performance was evaluated against the reference case, in which no LDs were introduced.

Overall, the results showed that installing LDs between the turbine spacings could substantially increase wind farm power output. In general, tandem placements were found to be more effective than staggered placements, achieving gains comparable to those obtained when LDs were integrated with the wind turbines themselves. Analysis of the vertical energy flux further indicated that the up-washing configurations were preferred over the down-washing ones, primarily because down-washing tended to trap exhausted wakes at lower altitudes – a behavior clearly identified with flow-field visualizations.

Despite providing a broad assessment of how different LD spatial patterns affected wind farm performance, this study had several limitations. First, it considered only a single wind direction, with the wind turbines and LDs in successive rows always aligned with the inflow. Future work should examine a broader range of wind directions to capture the aerodynamic interactions between wind turbines and LDs under more comprehensive scenarios. Second, although similar trends are observed, the two RANS turbulence models produce notably different predictions for LD effects and wake recovery, introducing uncertainties that are too large to support definitive quantitative conclusions. Experimental testing and numerical studies using higher-fidelity models are required to obtain more reliable power predictions, although such investigations demand substantially greater resources.

References

[1] Li Y, Yu W, Sciacchitano A and Ferreira C 2025 *Wind Energy Science* **10** 631–659
[2] Li Y, Fijen M, Dsouza B, Yu W, Sciacchitano A and Ferreira C 2025 *Wind Energy Science* **10** 3091–3124

[3] Broertjes T, Bensason D, Sciacchitano A and Ferreira C 2024 *Journal of Physics: Conference Series* vol 2767 p 072012

[4] Avila Correia Martins F, van Zuijlen A and Simão Ferreira C 2025 *Wind Energy Science* **10** 41–58

[5] Li Y, Yu W, Sciacchitano A and Ferreira C 2025 *Journal of Physics: Conference Series* vol 3016 p 012042

[6] Ferreira C, Bensason D, Broertjes T J, Sciacchitano A, Martins F A and Ajay A G 2024 *Journal of Physics: Conference Series* vol 2767 p 092107

[7] Watson S, Moro A, Reis V, Baniotopoulos C, Barth S, Bartoli G, Bauer F, Boelman E, Bosse D, Cherubini A *et al.* 2019 *Renewable and sustainable energy reviews* **113** 109270

[8] van der Laan M P, Andersen S J, Ramos García N, Angelou N, Pirrung G R, Ott S, Sjöholm M, Sørensen K H, Vianna Neto J X, Kelly M, Mikkelsen T K and Larsen G C 2019 *Wind Energy Science* **4** 251–271

[9] Veers P, Bottasso C L, Manuel L, Naughton J, Pao L, Paquette J, Robertson A, Robinson M, Ananthan S, Barlas T *et al.* 2023 *Wind Energy Science* **8** 1071–1131

[10] Vattenfall AB 2025 Horns Rev 1 `https://powerplants.vattenfall.com/horns-rev/` Accessed on 4th December 2025

[11] Selig M S, Guglielmo J J, Broeren A P and Giguere P 1995 *Summary of Low-Speed Airfoil Data: Volume 1* (SoarTech publications) ISBN 978-0-964-67471-4

[12] Barthelmie R J, Hansen K, Frandsen S T, Rathmann O, Schepers J, Schlez W, Phillips J, Rados K, Zervos A, Politis E *et al.* 2009 *Wind Energy* **12** 431–444

[13] Wu Y T and Porté-Agel F 2015 *Renewable Energy* **75** 945–955

[14] Li Y, Sciacchitano A and Yu W 2026 Case settings and selected results for CFD simulations in "Augmenting vertical energy entrainment within wind farms via lifting devices" URL `https://doi.org/10.4121/f0b7b52b-421b-4f2e-a231-173b131ae356`

[15] Manwell J F, McGowan J G and Rogers A L 2010 *Wind energy explained: theory, design and application* (John Wiley & Sons) ISBN 978-1-119-99436-7

[16] Calaf M, Meneveau C and Meyers J 2010 *Physics of fluids* **22** 015110

[17] OpenCFD Ltd 2025 OpenFOAM: User Guide v2506 `https://develop.openfoam.com/Development/openfoam/-/tree/OpenFOAM-v2506`

[18] Menter F R 1994 *AIAA journal* **32** 1598–1605

[19] Shih T H, Liou W W, Shabbir A, Yang Z and Zhu J 1995 *Computers & fluids* **24** 227–238

[20] Richards P and Hoxey R 1993 *Journal of wind engineering and industrial aerodynamics* **46** 145–153

[21] Hargreaves D and Wright N G 2007 *Journal of wind engineering and industrial aerodynamics* **95** 355–369

[22] Hansen K S, Barthelmie R J, Jensen L E and Sommer A 2012 *Wind Energy* **15** 183–196